Magnetic ordering in Ni-rich NiMn alloys around the multicritical point: Experiment and theory

Pampa Pal,* Rudra Banerjee, Radheshyam Banerjee, and Abhijit Mookerjee
Department of Condensed Matter and Materials Science, S. N. Bose National Centre for Basic Sciences, JD Block, Sector III, Salt Lake City, Kolkata 700098, India

Gopi Chandra Kaphle†
Department of Physics, Tribhuvan University, Kathmandu, Nepal

Biplab Sanyal, J. Hellsvik, and Olle Eriksson
Department of Physics and Astronomy, Uppsala University, Box 516, SE-75120 Uppsala, Sweden

P. Mitra and A. K. Majumdar
Indian Institute of Science Education and Research, Kolkata, Mohanpur Campus, Mohanpur 741252, Nadia, West Bengal, India

A. K. Nigam
Tata Institute of Fundamental Research, Homi Bhabha Road, Mumbai 400005, India

(Received 28 October 2011; revised manuscript received 28 March 2012; published 3 May 2012)

We have carried out an experimental study of Ni-rich NiMn alloys in a series of compositions across the multicritical point and determined the phase diagram within that range. We have observed ferromagnetic long-range order with reentrant spin-glass/ferro-spin-glass phase for $x \leqslant 25$, an antiferromagnetic long-range order around $x \sim 37$, and a gradual change from a canonical spin-glass state to a long-range antiferromagnetic phase in the intermediate composition region. In order to explain the experimental observations, we have examined the physical properties from a density functional based first-principals theoretical analysis and used it to understand the experimental results. Using atomic spin dynamics simulations based on the Landau-Lifshitz-Gilbert equation, we have found the aging behavior and anomalously slow relaxation of magnetization in the composition range where experiment observes spin-glassy behavior.

DOI: 10.1103/PhysRevB.85.174405 PACS number(s): 71.20.Be, 75.50.Lk, 71.70.Gm, 75.60.−d

I. INTRODUCTION

Magnetism in $Ni_{100-x}Mn_x$ (composition of Mn in atomic %) alloys provides a classic example of a disordered system with competing interactions. Magnetic parameters, such as transition temperatures, saturation magnetization, and coercivity, for different compositions are useful in assessing their application potentials.

In an early work, Hahn and Kneller[1] carried out magnetic studies on Ni-Mn alloys as a function of heat treatment. They found that in spite of quenching from well above the ordering temperature, there exists small ferromagnetically ordered Ni_3Mn regions of about 20 Å in diameter in a matrix of the disordered material. This made the preparation of homophase Ni-Mn alloys a difficult task.

Soon after, Kouvel and Graham[2] established the coexistence of ferromagnetism and antiferromagnetism coming from competing pair exchange interactions between the components at low temperatures in disordered $Ni_{100-x}Mn_x$ alloys with $x = 20$, 25, and 30, through hysteresis loop and torque measurements.

Kouvel *et al.*[3] reported the magnetic phase diagram in the composition range $23 \leqslant x \leqslant 27$. They observed, below the multicritical point (MCP) of $x = 23.9$ and $T = 102$ K, a double transition from a paramagnetic to a ferromagnetic state at T_C followed by a spin-glass (SG) like state at $T_{fg} < T_C$ with a reentrant character. Above $x = 23.9$ they found a paramagnetic to a normal SG state at T_g.

Aitken *et al.*[4] found the MCP to be above $x = 26$. This difference could arise from the difference in atomic short-range order in the two works. Hauser and Bernardini[5] studied sputtered films of $Ni_{100-x}Mn_x$ alloys and their bulk counterparts. They observed paramagnetic to spin-glass transition through ac susceptibility, χ measured at 10 kHz and 4 Oe ac field. Bulk samples with $x = 22$, 27, and 31 gave T_g of 40, 78, 73 K (much lower than 110 K found by Aitken *et al.*[4]) and the Curie-Weiss plot ($1/\chi$ vs T) for $x = 27$ gave a Néel temperature $\theta = 125$ K and n_{eff} of 2.5 μ_B which lies in between 0.3 and 3.2 μ_B found from neutron scattering experiments. It also gave a displaced hysteresis loop. Ferromagnetism disappeared at $x = 27$ since χ fell abruptly to 0.767×10^{-3} from 14.7×10^{-3} for $x = 22$ where $T_C \sim 290$ K and $T_g \sim 40$ K. They concluded that the presence of ferromagnetism below $x = 26$ is independent of preparation conditions, be they induction melted or quenched bulk alloy or sputtered films. However, the magnetic parameters such as T_C, T_g, and $\chi(T)$ varied considerably. Needless to say that a more detailed magnetic phase diagram of this interesting system is certainly necessary, especially away from the multicritical composition.

In the experimental part of this paper we have investigated in detail the magnetic properties of six samples of disordered $Ni_{100-x}Mn_x$ alloys enclosing the critical concentration ($x = 25$) in the composition range $x = 15$–37 at.% Mn which was the transition region from ferromagnetism to antiferromagnetism. For alloys with $x = 15$ and 20, on decreasing

the temperature, we observed a paramagnetic (PM) to a ferromagnetic (FM) transition at T_C and then below T_{fg} the occurrence of a spin-glass (SG) like phase. Previous theoretical studies[6,7] had also shown that this SG-like phase below T_{fg} may have a spontaneous FM moment with the transverse spin components ordered in a spatially random manner. It has therefore been called a "mixed phase." We indeed found that the SG-like phase has a spontaneous moment and the FM to SG-like transition temperature (T_{fg}) increased while the FM Curie temperature (T_C) decreased with increasing Mn concentration. They met at $x = 25$ and $T \sim 100$ K, the multicritical point (MCP). For alloys with $x = 30$ and 35, we observe only a single transition from paramagnetic to a spin-glass-like (or antiferromagnetic) phase which is different from that of the previous "reentrant spin-glass" phase. At higher concentrations such as $x = 37$, a paramagnetic to an antiferromagnetic transition is noticed.

We shall interpret the above behavior in terms of a Weiss field constructed out of the Ruderman-Kittel-Kasuya-Yoshida (RKKY) kind of indirect exchange interaction between the moments mediated by the conduction electrons as in an itinerant magnetic system rather than the pair interactions of a localized model. In this model the dominant exchange energies are antiferromagnetic Mn-Mn and ferromagnetic Ni-Ni and Ni-Mn interactions.[8] According to this model, for low Mn concentration (x), Mn-Mn interaction is negligible and hence all the spins become parallel resulting in an increase in M falling on the right segment of the Slater-Pauling (SP) curve (moment/atom vs electron/atom) with a slope of -1. For disordered alloys with somewhat higher x, the Mn-Mn AF interaction wins over the Ni-Mn FM interaction and Mn spins tend to cancel each other. As a result M decreases with x and starts following the left segment of the SP curve. At still higher x, the Ni $3d$ minority band gets gradually filled reducing the magnetization and due to the Z difference of 3 between Ni and Mn ferromagnetism is lost for $x \sim 30$, which is found in most experiments. The magnetic behavior of Ni-Mn alloys is typical of a competing interacting system with ferromagnetic and antiferromagnetic regions enclosing a concentration regime in which only magnetic short-range order (MSRO) exists.

II. EXPERIMENTAL PROCEDURE

Th electronic configuration of Ni is [Ar] $3d^8\ 4s^2$ and that of Mn is [Ar] $3d^5\ 4s^2$. The melting points of nickel and manganese are as high as 1455 °C and 1245 °C, respectively. Hence it is difficult to make homogeneous alloys with them as constituents. Ni-Mn alloys with 15, 20, 25, 30, 35, and 37 at.% Mn were arc melted in argon atmosphere with appropriate proportions of Ni and Mn. Then the ingots were homogenized for 3 days at 1000 °C and small cylindrical samples were spark cut for each composition. Their sharp corners were rounded off so that the demagnetization factor is reasonably uniform. Each sample was encapsulated in a quartz tube in argon atmosphere, annealed for 3 hours at 1000 °C, and then quenched in water. This treatment ensured the absence of an ordered Ni_3Mn phase which is strongly ferromagnetic ($T_C \sim 700$ K) but could not prevent some atomic short-range ordering. A final annealing was done in argon atmosphere at 1100 °C to reduce strain introduced due to cold rolling. We performed the magnetic measurements using a vibrating sample magnetometer (VSM), a superconducting quantum interference device magnetometer (SQUID, MPMS of Quantum Design), and a PPMS VSM of Quantum Design. The x-ray diffraction of the samples was carried out using a Philips XRD machine (X′Pert PRO Diffractometer) with a Guinier-type camera employing a focusing geometry and a solid-state detector. The radiation used was Cu $K_{\alpha 1}$. The chemical composition of the alloys was determined using standard analytical methods such as energy-dispersive x-ray analysis (EDAX).

III. EXPERIMENTAL RESULTS AND DISCUSSION

We have analyzed Ni-Mn alloys with Mn concentration varying from 15 to 37 at.%, in the range where it is expected to exhibit spin-glass behavior.[9]

A. Structural properties

XRD measurements revealed that all the alloys are of single face-centered-cubic phase. A typical XRD pattern for the $Ni_{85}Mn_{15}$ sample is shown in Fig. 1. Table I shows the measured lattice constants as a function of alloy composition. These lattice constants differ by only 1.4 to 2.8% from that of pure Ni.

We also note that the lattice constant increases monotonically with the increase of Mn concentration implying a good control of the alloy composition. As mentioned earlier, there are significant difficulties in forming the fully random alloy. The problem is the precipitation of a second phase of ordered $L1_2$ Ni_3Mn which is ferromagnetic with $T_C \sim 700$ K and lattice parameter $\sim$3.60 Å as against $\sim$3.57 Å for the disordered $Ni_{75}Mn_{25}$.

For any disordered system, there may be some local preferences between like or unlike atoms. This is called clustering or short-range order. Cowley[10] introduced a parameter α_i which is a measure of the average number of unlike nearest neighbors throughout the crystal. We have applied the Rietveld method to analyze the x-ray diffraction data to calculate this short-range order parameter of the $Ni_{75}Mn_{25}$ sample. By definition $\alpha_i = 1 - p_i/x_A$, where p_i is the probability that the

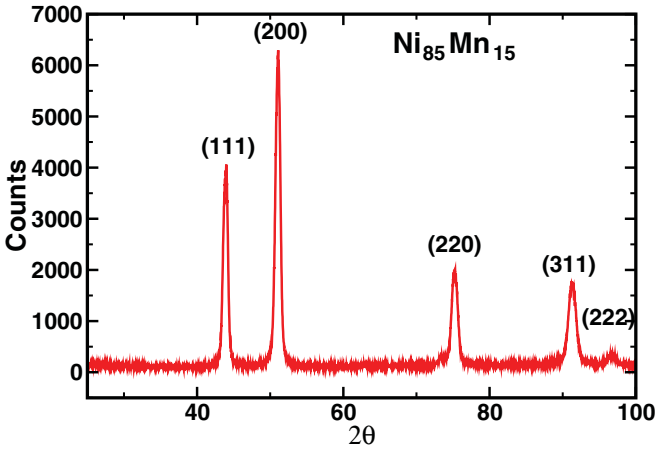

FIG. 1. (Color online) A typical XRD pattern ($x = 15$) showing that alloys in the composition range $15 \leqslant x \leqslant 37$ have single-phase face-centered-cubic structures.

TABLE I. Alloys studied and their lattice constants.

Mn Conc. (at.%)	Lattice Parameter (Å)
15	3.572 ± 0.004
20	3.583 ± 0.007
25	3.595 ± 0.007
30	3.615 ± 0.005
35	3.654 ± 0.006
37	3.670 ± 0.004

atomic site i is occupied by an A atom. The probability that we get from Rietveld analysis is 0.7373, which deviates from 0.75. Hence the value of the short-range order is given by $\alpha_i = 1 - (0.7373/0.75) = 0.0169$. Therefore the percentage of short-range order is ∼1.7%. Our alloys are definitely not "fully random" but contain ∼98.3% of disordered $Ni_{75}Mn_{25}$.

The point to note here is that the observed exotic complex mixture of magnetic phases that include short-range ordering, clustering, randomness on the nm scale, etc., do not affect our phase diagram. The small amount of ordered ferromagnetic Ni_3Mn phase (∼1.7%) only adds a small temperature-independent moment since $T_C \gg 300$ K. Our M vs H data for the MCP alloy ($x = 25$) at 300 K is a straight line passing through the origin like that of a paramagnet without any detectable hysteresis (see Fig. 2).

B. dc magnetization

Magnetization measurements $M(T)$ of $Ni_{100-x}Mn_x$ ($15 \leqslant x \leqslant 37$) samples were done in the temperature range of 5–350 K, both in low (∼20 Oe) and high (∼120 kOe) fields. For zero-field-cooled (ZFC) measurements, the samples were cooled down from 350 to 5 K in zero magnetic field. After cooling, a small field of 20 Oe was applied and held constant while M was measured as the temperature was raised slowly up to 350 K. Subsequently the temperature was lowered down to 5 K and the field-cooled (FC) data were taken while heating till 350 K. During this temperature cycle, $M(T)$ was quasistatically measured for finding the various transition temperatures as shown in Fig. 3. Many of the conclusions in this section are supported by the hysteresis loop data reported in next subsection on high-field magnetization.

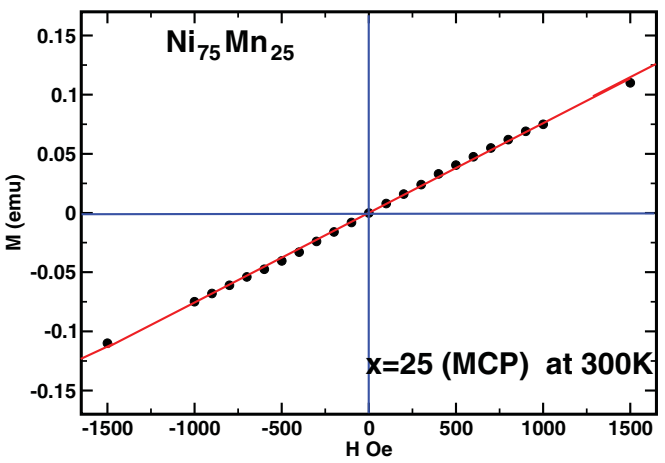

FIG. 2. (Color online) $M(H)$ data for the MCP alloy ($x = 25$) at 300 K showing paramagnetism without any detectable hysteresis.

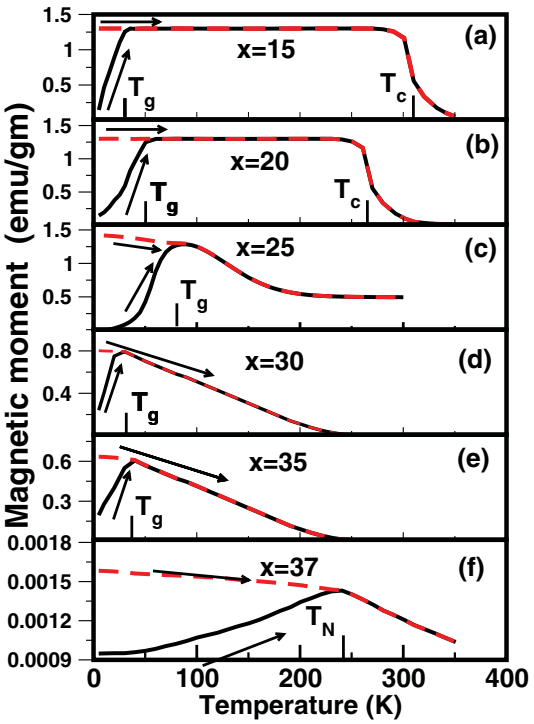

FIG. 3. (Color online) Magnetization vs temperature curves for Ni-Mn alloys between 5 and 350 K on heating after ZFC (black/full line) and then again heating after FC (red/dashed line) in a magnetic field of 20 Oe using a SQUID magnetometer. In the composition range $15 \leqslant x \leqslant 20$ we note that in addition to the para-ferro transition at T_C, there is a glassy transition at $T_g < T_C$ with a bifurcation between ZFC and FC curves. In the composition range $25 < x < 37$ the figure shows only a glassy transition. For $x > 37$ we see only a para-antiferro transition at T_N.

We see from Fig. 3 that for alloys with $x = 15$ and 20, ZFC and FC $M(T)$ curves show irreversibility in the low-temperature region. As T increases from 5 K, there is a bifurcation between ZFC and FC $M(T)$ curves at T_{fg} indicating a transition from a reentrant ferro SG-like state to a ferromagnetic state. In the intermediate temperature range, both ZFC and FC $M(T)$ remain constant almost until T_C is reached, as found from the dip in dM/dT vs T plots (not shown here), which is the point of inflection of the $M(T)$ vs T curve. This is in contrast to the concave $M(T)$ curve beyond the kink points in Fig. 1 of Ref. 1, for $x = 23$ and 23.5. At low temperatures, our alloys with $x = 15$ and 20 exhibit a reentrant/ferro spin-glass-like mixed phase having a spontaneous FM moment as well as glassy behavior below T_{fg} [as seen from $M(H)$ curves at 5 K in the next subsection]. The sample with $x = 15$ has $T_{fg} = 37$ K and $T_C = 310$ K while the sample with $x = 20$ has $T_{fg} = 60$ K and $T_C = 270$ K. This "reentrant" phase having a "mixed" character was predicted theoretically[6] long back and involves below T_{fg} a SG ordering of the spins transverse to the coexisting FM moments, while in the FM state above T_{fg} the transverse SG ordering is absent and only the FM alignment of the longitudinal spin components remains. It must be stressed here that this coexistence of FM and SG phase below T_{fg} is

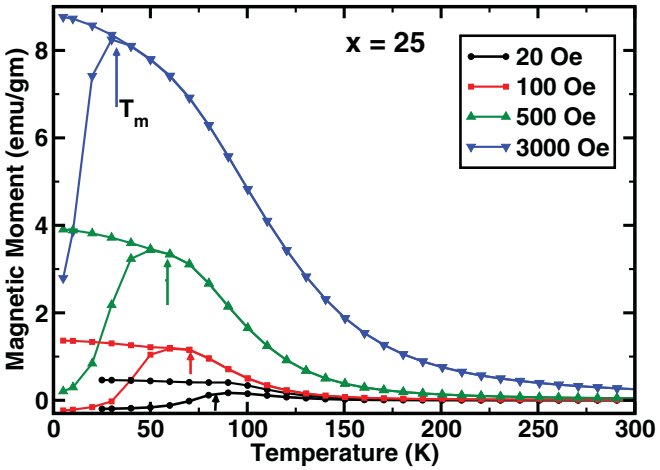

FIG. 4. (Color online) Zero-field-cooled (ZFC) and field-cooled (FC) magnetization curves at $H = 20$, 50, 200, and 3000 Oe for the alloy $Ni_{75}Mn_{25}$ at the MCP on the phase diagram. We note that at this composition there is a para-spin-glass transition at $T_g \sim 75$ K with a bifurcation between the ZFC and FC curves.

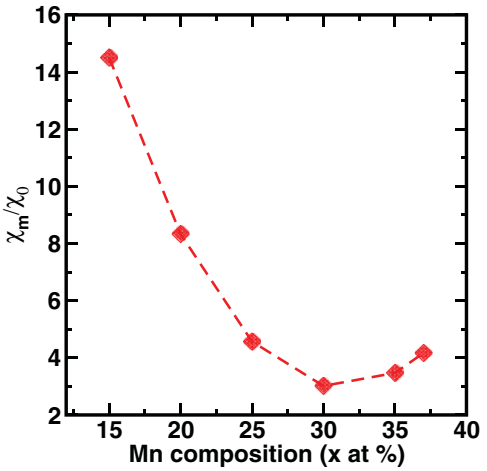

FIG. 5. (Color online) χ_m/χ_0 vs Mn concentration (at.% Mn) in $Ni_{1-x}Mn_x$ alloys. At $x = 25$ (MCP) this ratio approaches the value ~4.4 characteristic of spin glasses. The ratio increases either as ferro- or antiferromagnetism sets in.

not a spatially segregated coexistence of infinite ferromagnetic clusters decoupled from finite clusters. The coexistence takes place over the whole sample. The FM ordering persists down to the lowest temperatures ($T \ll T_{fg}$). AuFe[11,12] is the first system where the coexistence was observed just below the percolation threshold of 15 at.% Fe. $Fe_{80-x}Ni_xCr_{20}$ ($10 \leqslant x \leqslant 30$) alloys, with a variation of Ni from 10–30 at.% at the cost of Fe with Cr remaining fixed, is another system, similar to the present NiMn, which offered a unique opportunity of observing various magnetic phases such as ferromagnetic, mixed ferro-spin-glass, spin-glass, and antiferromagnetic.[13–15] Here the dominant competing interactions are from FM Ni-Ni and Ni-Cr, and AF Cr-Cr interactions which produce FM-SG-like coexisting phases.

We associate the lower temperature transition at T_{fg} for $x = 15$ and 20 and the single transition at the MCP for $x = 25$ with a spin-glass-like phase. Figure 4 focuses on the zero-field-cooled (ZFC) and field-cooled (FC) magnetization curves at $H = 20$, 50, 200, and 3000 Oe for the MCP alloy $Ni_{75}Mn_{25}$. We find a gradual shift of T_m [where ZFC $M(T)$ shows a peak] toward lower temperatures at higher external fields. The ZFC peak at T_m in the SG-like state is due to the gradual unfreezing of moments which allows the magnetic field to align them. Beyond T_m we observe the paramagnetic $\sim 1/T$ fall for both the ZFC and FC $M(T)$ and hence no irreversibility for $T > T_m$. At higher applied fields the magnetic field itself tends to disrupt the freezing and hence thermal defreezing is effective only till a gradually lower value of T_m. This approaches the glass-transition temperature T_g as $H \to 0$.

The samples with $x = 25$, 30, 35, and 37 have only one type of transition which can be clearly seen from the steep rise in the $M(T)$ curves [Figs. 2(c)–2(f)] until a maximum is reached and then a clear knee indicating a paramagnetic to a spin-glass-like (PM-SG)/antiferromagnetic (AF) transition. T_g/T_{fg} for $x = 25$ is 100 K and T_g of $x = 30$ is 29 K. $T = 40$ K for $x = 35$ may be a spin-glass freezing temperature or a Néel temperature (T_g/T_N) whereas for $x = 37$, 237 K is clearly the Néel temperature T_N, since the moment decreases abruptly at this concentration from 0.6 to 0.0016 emu/g as x changes from 35 to 37. For $x = 30$–37, the spin-glass-like/antiferromagnetic state goes directly to the paramagnetic one without passing through any intervening ferromagnetic phase.

In Fig. 5, the ratio χ_m/χ_0 versus Mn concentration (at.% of Mn) is plotted, where χ_m and χ_0 are the demagnetization-corrected low-field susceptibilities (after zero-field cooling) at the maximum values and at 5 K, respectively. We find that the ratio value decreases with increasing x. It is as large as ~15 for $x = 15$ indicating a long-range ferromagnetic order, while at $x = 25$, the ratio ~4.4 which is typical of a canonical spin glass. It is interesting to note that subsequently the value of the ratio reaches a minimum around 35 at.% Mn and then it starts increasing indicating the onset of another long-range order (here antiferromagnetic).

C. High-field magnetization and hysteresis loops

Hysteresis loops were obtained for each sample after cooling in zero fields to 5 K from above $T_C/T_{fg}/T_g/T_N$ and measured in fields up to 50 kOe using the vibrating-sample magnetometer. In Fig. 6 we have plotted the magnetization of all six samples at 5 K till 16 kOe. They show drastic changes with Mn content. For the samples with $x = 15$ and 20, 16 kOe was sufficient for magnetic saturation. In the case of $x \geqslant 25$, the magnetization was still rising at the highest attainable field of 120 kOe, as shown in the inset of Fig. 5, top panel for $x = 25$. The reentrant/ferro spin-glass-like mixed phases for $x = 15$, 20, and 25 have spontaneous FM moments below T_{fg}. This is seen clearly from their respective values of H_C of 30, 90, and 400 Oe at 5 K which is much less than their T_{fg} of 37, 60, and 100 K, respectively. Finally their H_Cs tend to zero above their T_Cs of 311, 270, and 100 K, respectively. The increase of H_C with Mn is what is expected. H_C increases with the increase of impurity content and the associated lattice strain.

When x increases beyond $x = 25$, the $M(H)$ curves spread out. At $x = 25$ (top panel of Fig. 6), we get hardly any magnetic saturation and this locates the critical point. The bell-shaped low-field region for $x = 25$ resembles those observed in spin

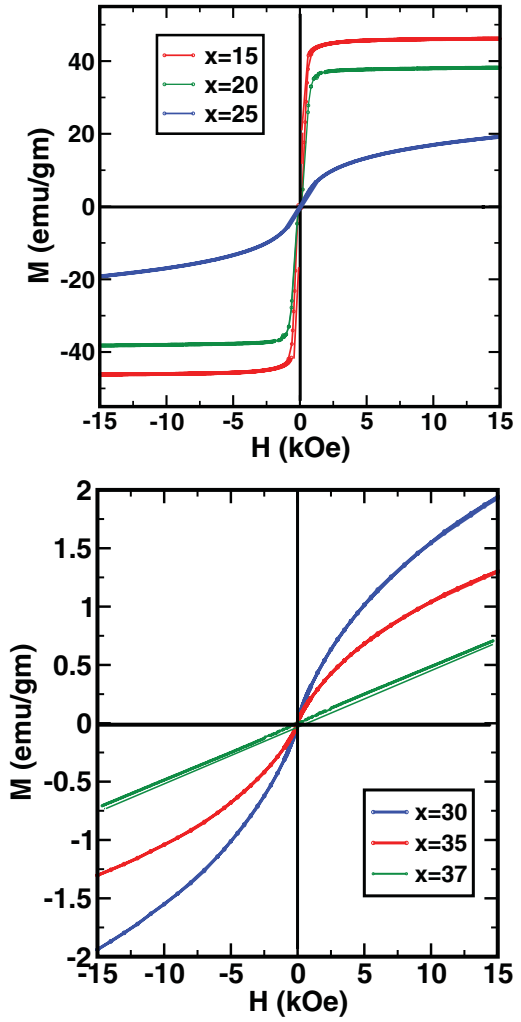

FIG. 6. (Color online) Magnetization measured at low temperatures (5 K) as a function of applied fields H. In the composition range $x < 25$ the hysteresis with saturation at high fields is characteristic of ferromagnetism. At the MCP ($x = 15$) the hysteresis curves do not saturate and resemble those for spin glasses. For $15 < x < 37$ the hysteresis again is characteristic of spin glasses, until at $x > 37$ it becomes almost linear, indicating antiferromagnetism.

glasses but the sample still retains a high susceptibility at low temperatures. For lower values of x, the $M(H)$ curves saturate at fields ~1 kOe like those of ferromagnets but with the increase of x, the lack of saturation gradually becomes more evident and finally around $x = 37$ their curvature disappears and $M(H)$ becomes almost linear implying antiferromagnetic character (bottom panel of Fig. 6).

D. ac susceptibility

ac susceptibility (χ_{ac}) was measured in $Ni_{100x}Mn_x$ alloys with $x = 25$, 20, and 30 after ZFC to 5 K from 300 K and measuring in small ac fields of 1 Oe at 2.9, 29, 290, 590, and 601 Hz and 5 Oe (at ~100 to 10 000 Hz) using MPMS and PPMS, respectively, for probing the possible spin-glass-like ordering observed in dc $M(H,T)$ studies. The spin-freezing temperatures of the alloys were estimated from $\chi_{ac}(T)$. They agreed reasonably well with those found from the dc measurements. We discuss here in detail the MCP alloy together with $x = 20$ and 30.

(i) $x = 25$ (MCP). $Ni_{75}Mn_{25}$ is the most interesting as well as complicated composition because it is the MCP with three coexisting magnetic phases. Figure 6 shows the real part of ac susceptibility $\chi'(T)$ (emu) vs T at several frequencies. All of them have rounded maxima around 100 K; the lowest frequency has the highest $\chi'(T)$ which is rather obvious since at low frequencies clusters of all sizes respond to magnetic fields whereas at high frequencies only the smaller clusters do. They converge to a nonzero $\chi'(T)/\chi'(T_g)$ of ~0.1 as $T \rightarrow 0$ K and are frequency independent above T_g. In canonical spin glasses, say, CuMn (4.4 at.%), $\chi'(T)/\chi(T_g) \sim 0.5$ as $T \rightarrow 0$ K.

As shown in the bottom panel of Fig. 7 (which is the top panel on an expanded scale), there is an increase in T_g of ~2 K around 100 K with a 200-fold increase in frequency from 3 to 600 Hz. For canonical spin glasses T_g decreases with increasing frequency since the smaller clusters have lower freezing temperature. Many of the above features in $x = 25$ are not typical in canonical spin glasses since after all $x = 25$ and $T \sim 100$ K is the MCP where spin-glass, ferro-spin-glass, and ferromagnetic phase boundaries intersect.

Measuring $\chi'(T)$ in ac fields of 5 Oe between 10 and 300 K using the PPMS we get what is shown in Fig. 8. Here $\Delta T_g \sim 7$ K around 100 K as the frequency changes from ~100 to 5000 Hz.

The imaginary part χ'', the absorption part of the susceptibility, is the Fourier transform of the two-spin correlation function which characterizes the dynamics of the magnetic system. χ'' is expected to show some anomaly near the magnetic phase transitions. χ'' extrapolates to ~50% of its peak value as $T \rightarrow 0$ in CuMn and AgMn spin glasses but in EuSrS, this extrapolates to zero as $T \rightarrow 0$. Figure 9 shows the imaginary part of ac susceptibility χ''(emu) vs T for $x = 25$ at several frequencies, measured with an MPMS and a PPMS, respectively. The peaks are much sharper than those of χ'. χ'' extrapolates to zero as $T \rightarrow 0$ as in EuSrS. Also their magnitudes increase with frequency as in many SGs. χ'' shifts by ~10 K from 80 K for ~3 to 600 Hz (MPMS) and 14 K for ~100 to 5000 Hz (PPMS). So, $T = 100$ K is indeed the multicritical temperature as found from dc measurements.

(ii) $x = 20$ (ferro-spin-glass). Figure 10 plots χ' vs T showing clearly the standard increase in T_{fg} with frequency and $\Delta T_{fg} \sim 12$ K (62 to 74 K) in the frequency range 111–9997 Hz. This confirms that $T_{fg} \sim 60$ K as found from dc measurements.

(iii) $x = 30$ (canonical spin-glass). The zero-dc field ac susceptibility of $Ni_{70}Mn_{30}$ was done with an ac drive field of 5 Oe between 11 and 7111 Hz. From the temperature dependence of the in-phase (χ') (not shown here) and the out-of-phase (χ''), we notice a steep rise around 18 K (Fig. 11) which is not too different from T_{fg} (29 K) found from the dc data. It is quite clear that different thermal treatment (quenching) might lead to different T_g/T_{fg}, but T_C is too robust to be affected by Ni_3Mn ordered phase, if present. The cusplike peak of the χ'' vs temperature curve and the dependence of the location of the cusp on frequency confirms the spin freezing. χ'' increases with frequency as expected.

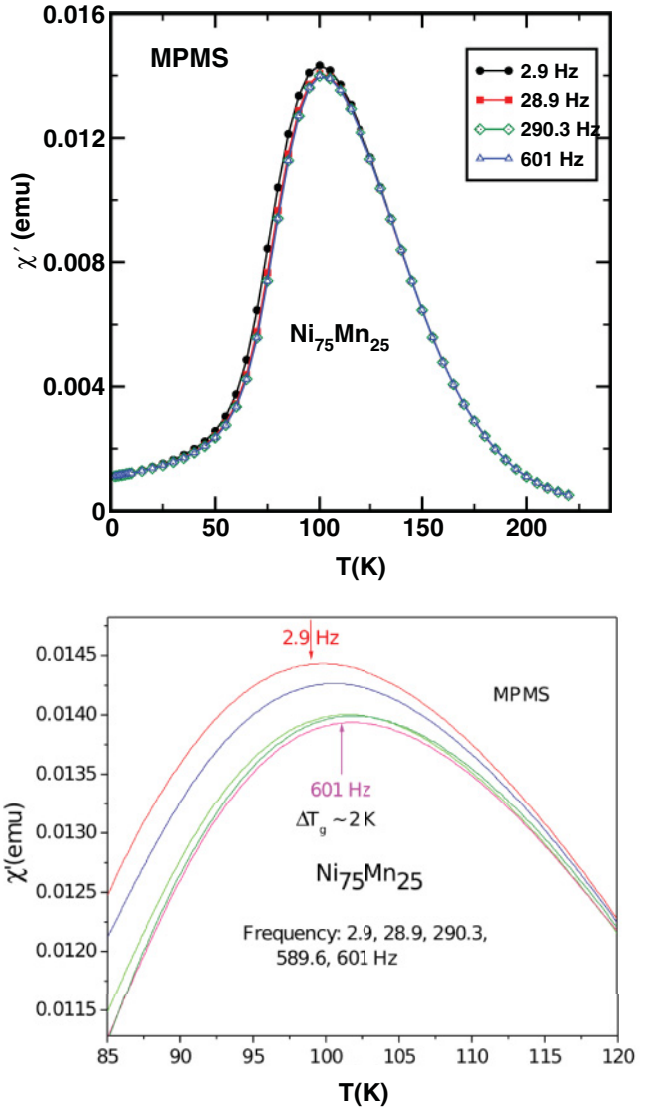

FIG. 7. (Color online) Top panel: Real part of ac susceptibility χ' (emu) vs T between 10 and 300 K for $x = 25$ at several frequencies using MPMS. The frequencies chosen were $\nu = 2.9$, 28.9, 290.3, 601 Hz. Bottom panel: Same as top panel, on an expanded scale between 85 and 120 K for $x = 25$ for illustrating the frequency dependence of T_g.

E. Magnetic relaxation

Thermoremanent magnetization is a thermally activated process. When the applied magnetic field is removed, the magnetization tries to approach the remanent magnetization in order to minimize the energy of the system. A magnetic field of 100 Oe was applied to the sample at 300 K and the sample cooled down to the measuring temperature. After the temperature was stabilized, the magnetic field was set to zero and the magnetization vs time $M(t)$ measurements were started and continued for about 13 000 s. Figure 12 plots the experimental time decay of normalized magnetization $\ln[M(t)/M(0)]$ for $0 < t < 10\,000$ s for $Ni_{75}Mn_{25}$ alloy at different temperatures. The magnetization shows anomalous slow relaxation as we approach and cross the glass-transition temperature. Around and below 70 K, although for long times

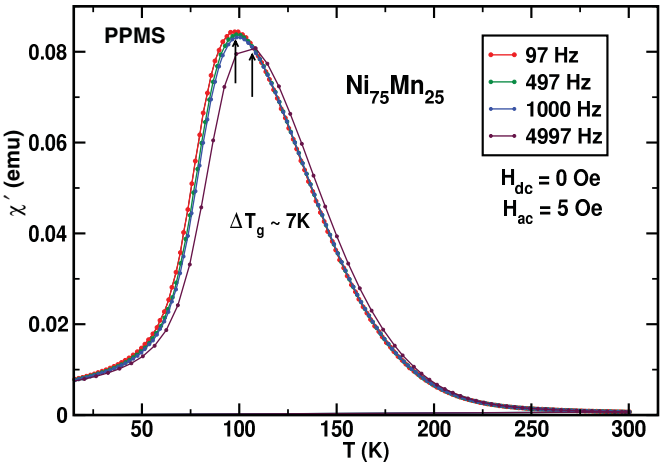

FIG. 8. (Color online) Real part of ac susceptibility χ' (emu) vs T for $x = 25$ at several frequencies between 100 and 5000 Hz using PPMS. The frequency dependence of ac susceptibility is clear at these higher frequencies and using a different setup as compared to Fig. 7.

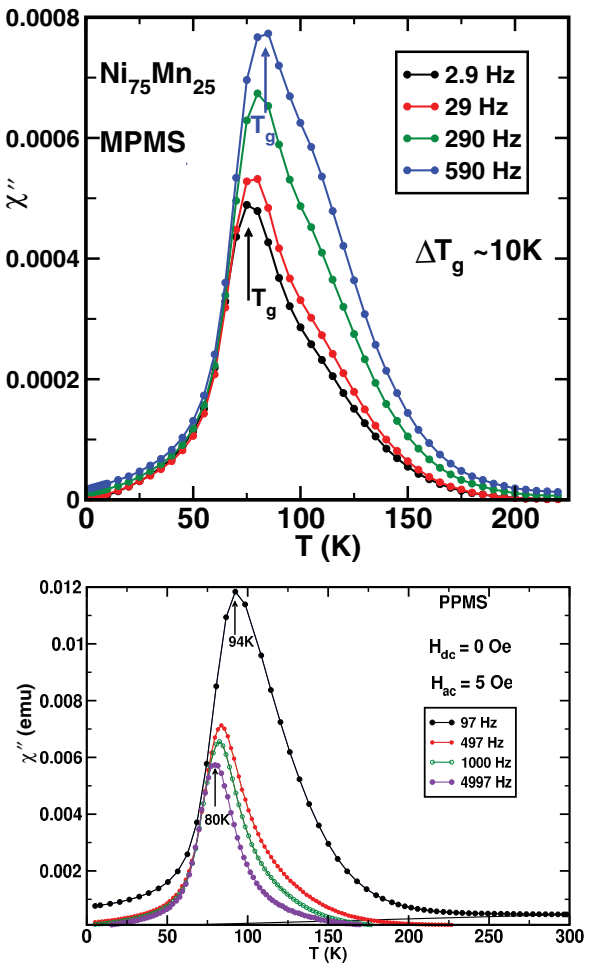

FIG. 9. (Color online) Imaginary part of ac susceptibility χ'' (emu) vs T for $x = 25$ at several frequencies between 100 and 5000 Hz using (top) MPMS and (bottom) PPMS. Both show that the anomaly at T_g is strongly frequency dependent.

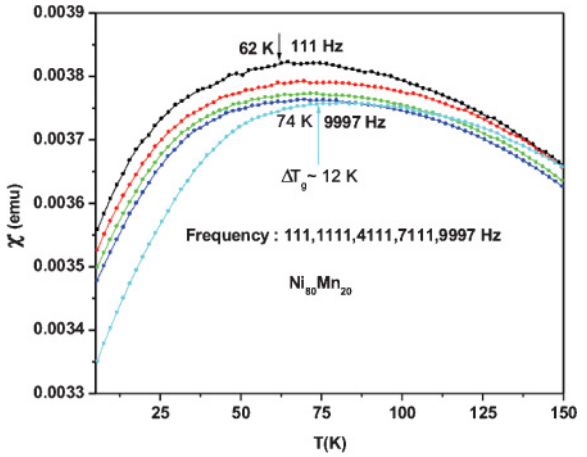

FIG. 10. (Color online) Plot of χ' vs T for $x = 20$, using a PPMS, shows that T_{fg} increases with frequency.

(>6000 s) $\ln[M(t)/M(0)]$ can be fitted to a line; its slope is so small that anomalous slow (power law or logarithmic) decay is suggested.

F. Experimental phase diagram

Figure 13 shows the magnetic phase diagram of disordered $Ni_{1-x}Mn_x$ alloys showing ferromagnetic (FM), ferro-spin-glass (FSG), conventional (canonical) spin-glass (SG), paramagnetic (PM), and antiferromagnetic (AFM) regions. The values of T_C, T_{fg}, T_g, and T_N are taken from Fig. 3 ($H = 20$ Oe). The lines joining the first three all meet at a point which is called the multicritical point (MCP; $x = 25$, $T = 100$ K). Beyond the MCP, at higher at.% of Mn, the spin-glass state directly goes to the paramagnetic state (up to 30 at.% Mn) or the antiferromagnetic state to the paramagnetic state (for 35 and 37 at.% Mn) with no intervening ferromagnetic phase. Beyond $x = 25$ till 30, T_g goes down; then at 35 there is a slight increase in the bifurcation temperature while M gradually decreases all the way (from ~1 to 0.6 emu/g). However, according to the neutron diffraction work[16] long-range antiferromagnetism does not set in for $x = 30$ but 35 at.% Mn is

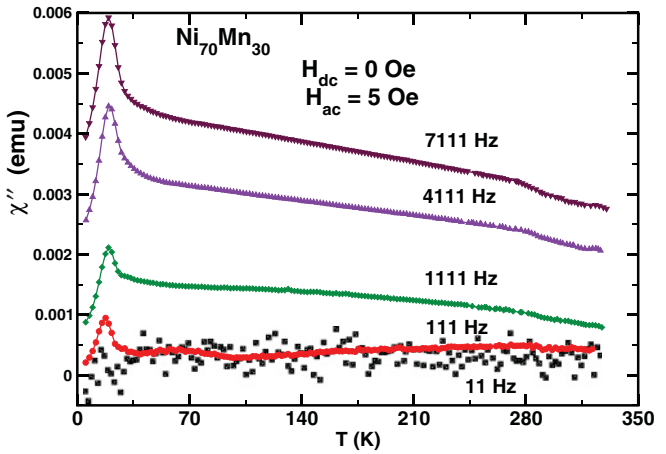

FIG. 11. (Color online) Imaginary part of ac susceptibility χ'' (emu) vs T for $x = 30$ with different frequencies using PPMS. The results indicate a canonical para to spin-glass transition.

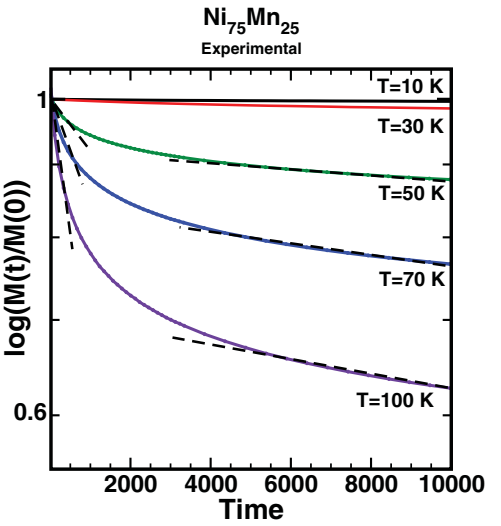

FIG. 12. (Color online) Experimental study of time decay of magnetization for the $Ni_{75}Mn_{25}$ alloy at different temperatures. The alloy magnetization shows anomalously slow relaxation as we approach and cross the glass-transition temperature below 100 K. Below 100 K we can no longer fit data with exponential decay functions.

indeed antiferromagnetic but T_N could not be found because of the weak Bragg peak and the temperature-dependent diffuse scattering. For lower values of x, below the multicritical point, the samples pass through two phases—ferromagnetic (FM) and reentrant spin-glass or ferro-spin-glass. In reentrant spin-glass (RSG or FSG) systems, with decreasing temperature one observes a paramagnetic-ferromagnetic transition at T_C. Then at a lower temperature T_{fg}, spin-glass-like properties show up. In the phase diagram we get a critical concentration which is the point ($x = 25$) where T_C and T_{fg} (100 K) come together. We further note that the value of T_{fg} increases and T_C decreases with increasing x. The variation of T_g with Mn concentration is very interesting. Up to $x = 30$, it decreases linearly with increasing x, then we get T_N in place of T_g signifying AFM order which increases with Mn concentration. The boundary between the reentrant/ferro-spin-glass (FSG) and the canonical spin-glass (SG) phases is a vertical line which touches the multicritical point ($x = 25$).

The phase diagram that we obtained from magnetization data shows an interesting concentration range ($15 \leqslant x \leqslant 25$) in which the system undergoes two magnetic transitions on

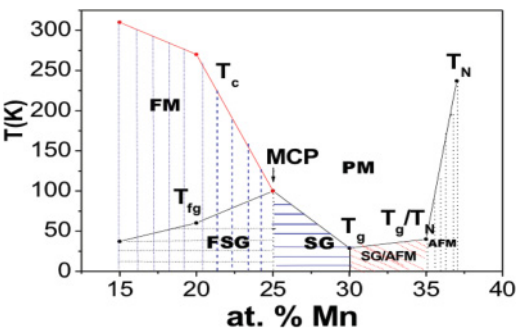

FIG. 13. (Color online) Experimental phase diagram.

lowering the temperature: from paramagnetism to ferromagnetism and from ferromagnetism to a spin-glass-like state. For ($25 \leqslant x \leqslant 35$), however, only paramagnetic to spin-glass-like transition is observed and $x = 37$ shows only one transition but that is from antiferromagnetic to a spin-glass state. Since the magnetic properties of quenched Ni-Mn alloys depend strongly on composition around 25 at.% Mn, it is essential to ensure an accurate determination of composition. We find (inset of Fig. 1) that the lattice parameter increases monotonically with x and shows no anomaly as the magnetic state widely changes from a mixed FM-SG-like state to an AFM one. So, we have taken EDAX (energy dispersive x-ray analysis) of every sample and got satisfactory results.

IV. THEORETICAL ANALYSIS

A. Electronic structure

For a first-principles theoretical analysis we obtained an accurate electronic structure of these alloy systems. This involves two steps: first a density functional based derivation of the Hamiltonian "potential parameters" and structure matrix which describe the chemistry and crystallography of the alloy. Second, we need an accurate technique to deal with the disorder in the system and averaging over the disordered configurations. For the former we have chosen the tight-binding linear muffin-tin orbital (TB-LMTO) method[17] and for the latter the augmented space recursion (ASR) formalism.[18] This formalism gives a prescription of how to obtain the configuration average of Green's and response functions in a disordered system by downfolding onto a specific subspace of the configuration space. Details have been discussed in detail in a monograph.[19] This method goes beyond the single-site, mean-field coherent potential approximation (CPA) and three of the successful generalizations of the CPA are based on this theorem (traveling cluster CPA,[20] itinerant CPA,[21] and cluster CPA).[22,23] The configuration-averaged Green's function $\langle\langle G^{\sigma}_{\vec{R}_i L \vec{R}_i L}(E)\rangle\rangle$ leads to the local density of states, the charge and magnetization densities and the local magnetic moment per atom:

$$
\begin{aligned}
n^{\sigma}(E,\vec{R}_i) &= -\frac{1}{\pi}\mathrm{Im}\langle\langle G^{\sigma}_{\vec{R}_i L \vec{R}_i L}(E + i\delta^{+})\rangle\rangle, \\
\rho^{\sigma}(\vec{r} - \vec{R}_i) &= \int_{-\infty}^{E_F} dE\, |\Phi(\vec{r} - \vec{R}_i, E)|^2 n^{\sigma}(E,\vec{R}_i), \qquad (1) \\
m(\vec{R}_i) &= \int_{AS} d^3\vec{r}\{\rho^{\uparrow}(\vec{r} - \vec{R}_i) - \rho^{\downarrow}(\vec{r} - \vec{R}_i)\}.
\end{aligned}
$$

Here $\vec{R}_i$ labels an atomic sphere around an ion core sitting at the site i, L are the angular momentum quantum numbers (ℓ,m), σ is the spin label, and AS is the atomic sphere $|\vec{r} - \vec{R}_i| < r_0$.

The interesting result that comes out of these calculations is the composition variation of the average *local* magnetic moment per atom. This is something we can compare with experiments and ascertain whether our electronic structure method is appropriate for further study. Figure 14 shows this comparison to be satisfactory within the limits of our approximation and gives us confidence for the next step.

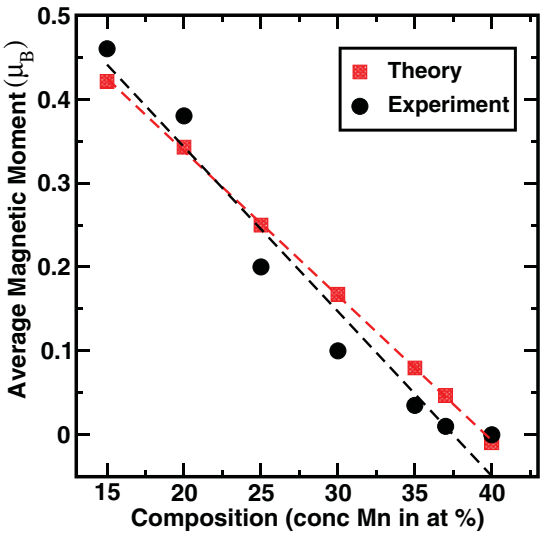

FIG. 14. (Color online) Experimental and theoretical magnetic moments as functions of composition.

B. Ordering of magnetic moment carrying atomic spheres

In order to understand the onset of magnetic ordering in random alloys, we proceeded in two steps. The formation of a magnetic moment within an atomic sphere was analyzed using the TB-LMTO-ASR as described above. This is an itinerant electron picture. The ordering of these moments is studied by mapping the problem to a Heisenberg model and deriving the exchange interactions, from the "effective pair energies" (EPE) obtained from the generalized perturbation approach (GPM).[24] This approach is well documented and we shall refer the reader to the cited paper for details.

$$
\Delta E = H = -\frac{1}{2}\sum_{\vec{R}_i, Q}\sum_{\vec{R}_j, Q'} J^{QQ'}(|\vec{R}_i - \vec{R}_j|)\vec{S}^{Q}_{\vec{R}_i}\cdot\vec{S}^{Q'}_{\vec{R}_j}. \qquad (2)
$$

The "spin" variables $\vec{S}_{\vec{R}_i}$ are now classical vectors with unit length. $\vec{R}_i$, as before, labels the atomic spheres and Q decides what type of constituent, A or B, occupies that site in a disordered binary alloy. Since $J^{(2)QQ'}_{\vec{R}_i,\vec{R}_j}$ are very small energy differences (of the order of mRy) of large energies (of the order of 10^3 Ry), a separate calculation of each component energy will produce errors larger than the small differences themselves. These interatomic "pair-exchange" parameters will be calculated following the theory of Lichtenstein *et al.*[25,26] For a Heisenberg model we shall begin the spin perturbation on a disordered local moment state (rather than a paramagnet):

$$
\begin{aligned}
J^{QQ'}(|\vec{R}_i - \vec{R}_j|) = \frac{1}{4\pi}\int_{-\infty}^{E_F} dE\, \mathrm{Im}\, m\mathrm{Tr}_L\big\{\Delta^{Q}_{\vec{R}_i}\ldots \\
\ldots T^{\uparrow\uparrow}(\vec{R}_i - \vec{R}_j)\Delta^{Q'}_{\vec{R}_j} T^{\downarrow\downarrow}(\vec{R}_j\vec{R}_i)\big\}, \qquad (3)
\end{aligned}
$$

where $\Delta^{Q}_{\vec{R}_i} = t^{-1}_{\vec{R}_i,Q\uparrow} - t^{-1}_{\vec{R}_i,Q'\downarrow}$. t is the on-site scattering matrix whereas T is the scattering path operator which is related to the

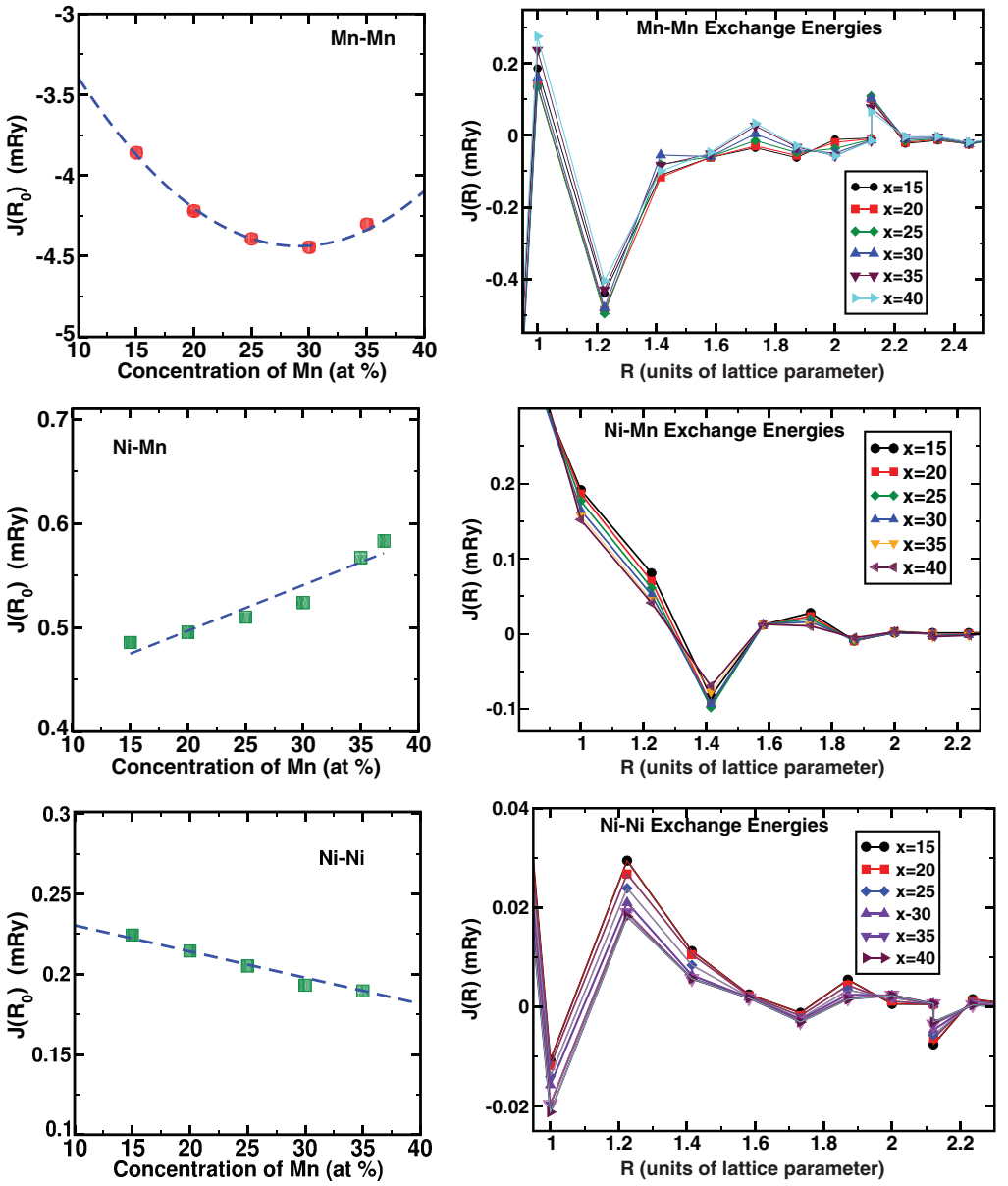

FIG. 15. (Color online) EPE for Ni_xMn_{1-x} alloy. Left column: EPE for the nearest-neighbor distances. It is seen that the Mn-Mn EPE is antiferromagnetic and most dominant, whereas those for Mn-Ni and Ni-Ni are ferromagnetic but relatively weak. Right column: EPE for second-nearest neighbor and further distances. The oscillatory behavior shows the possibility of frustration.

off-diagonal element of the Green's function. Ferromagnetic and antiferromagnetic interactions are represented by positive and negative values of $J^{QQ'}(|\vec{R}_i - \vec{R}_j|)$.

We have calculated EPE on a $40 \times 40 \times 40$ lattice. Mn-Mn, Mn-Ni, and Ni-Ni EPE show oscillatory behavior with distance, and nearest-neighbor Mn-Mn EPE is antiferromagnetic whereas Mn-Ni EPE and Ni-Ni EPE are ferromagnetic. This is a clear indication of strong frustration in the system. The $J^{\mathrm{NiNi}}(0)$ increases with increase of Ni concentration, consistent with the fact that Ni has very fragile magnetic moment and depends heavily on its surroundings. When Ni concentration is high, its more likely to be surrounded with more Ni atoms and the dominant $J^{\mathrm{NiNi}}(0)$ increases. On the other hand the dominant EPE for both Mn-Mn and Mn-Ni decreases with increase of Ni concentration (see Fig. 15).

C. Mean-field and Monte Carlo analysis of the random Heisenberg model

Our analysis will begin with the random Heisenberg model shown in Eq. (2). Here $\vec{R}_i, \vec{R}_j$ refer to the sites on a face-centered-cubic lattice, Q, Q' refer to the type of atoms occupying the sites $\vec{R}_i$ and $\vec{R}_j$. In our case Q, Q' are either Ni or Mn. In the case of Mn-rich alloys where the dominant nearest neighbor $J^{\mathrm{MnMn}} < 0$, we partition the lattice into two sublattices $\mathcal{L}_1$ and $\mathcal{L}_2$ such that the nearest neighbor of a site in $\mathcal{L}_1$ is in $\mathcal{L}_2$ and vice versa. In the fcc lattice it is a layered

$L1_0$ arrangement. We now define a staggered local spin $\widehat{\sigma}_i$ and a staggered interaction $\widehat{J}^{QQ'}$ as

$$\widehat{\vec{S}}^{Q}_{\vec{R}_i} \cdot \widehat{\vec{S}}^{Q'}_{\vec{R}_j} = I_{ij} \vec{S}^{Q}_{\vec{R}_i} \cdot \vec{S}^{Q'}_{\vec{R}_j}$$
$$\text{and} \quad \widehat{J}^{QQ'}(|\vec{R}_i - \vec{R}_j|) = I_{ij}\, J^{QQ'}(|\vec{R}_i - \vec{R}_j|),$$

where $I_{ij} = \pm 1$ according to whether $\vec{R}_i, \vec{R}_j$ are in same or different sublattices. We shall rewrite the Hamiltonian in terms of the staggered quantities:

$$H = -\frac{1}{2} \sum_{\vec{R}_i} \sum_{\vec{R}_j} \widehat{J}^{QQ'}(|\vec{R}_i - \vec{R}_j|)\, \widehat{\vec{S}}^{Q}_{\vec{R}_i} \cdot \widehat{\vec{S}}^{Q'}_{\vec{R}_j} \tag{4}$$

but now the dominant staggered nearest neighbor $\widehat{J}^{\,\mathrm{MnMn}} > 0$.

The subsequent analysis will closely follow the arguments of Mookerjee and Roy.[27] This approach follows that suggested earlier by Kaneyoshi,[28] Plefka,[29] and Thouless *et al.*[30] We shall state here the final result and refer the curious reader to the above references.

The single-site mean-field approximation leads to local random Weiss fields given by

$$\vec{h}^{Q}(\vec{R}_i) = \sum_{Q'} \sum_{\vec{R}_j} J^{QQ'}(R_{ij})\, \vec{m}^{Q'}(\vec{R}_j), \tag{5}$$

where $R_{ij} = |\vec{R}_i - \vec{R}_j|$. Using Radon transforms we obtain the probability density of the random Weiss fields:[27]

$$P^{Q}\left(h^{Q}_{\mu}(\vec{R}_i)\right) = \left[(2\pi)^3 J^{Q}_{1\parallel} (J^{Q}_{1\perp})^{1/2}\right]^{-1} \exp\left[-\left(h^{Q}_{x} + h^{Q}_{y}\right)^2 \Big/ 2J^{Q}_{1\perp} - \left(h^{Q}_{z} - J^{Q}_{0}\right)^2 \Big/ 2J_{1\parallel}\right], \tag{6}$$

where P_0 is the normalizing factor and

$$J^{Q}_{0\mu} = \sum_{Q'} x_{Q'} m^{Q'}_{\mu} \sum_{R} J^{QQ'}(R),$$
$$J^{Q}_{1\mu\nu} = \sum_{Q'} x_{Q'} q^{Q'}_{\mu\nu} \sum_{R} \{J^{QQ'}(R)\}^2,$$
$$U^{T}_{\mu\nu} q^{Q}_{\nu\gamma} U_{\gamma\xi} = q^{Q}_{\mu} \delta_{\mu\xi}, \quad U^{T}_{\mu\nu} J^{Q}_{1\nu\gamma} U_{\gamma\xi} = J^{Q}_{1\mu} \delta_{\mu\xi},$$

where $h^{Q} = |\vec{h}^{Q}|$ and $F^{Q}(x) = \{L^{Q}(x)\}^{-1} \partial L^{Q}(x)/\partial x$.

$$m^{Q} = \int \Pi_{\mu} dh^{Q}_{z}(\vec{R}_i)\, \mathcal{P}\left(h^{Q}_{\vec{R}_i}\right) \left(h^{Q}_{z}/h^{Q}\right) F^{Q}(\beta h^{Q}),$$
$$q^{Q}_{\parallel} = \int \Pi_{\mu} dh^{Q}_{z}(\vec{R}_i)\, \mathcal{P}\left(h^{Q}_{\vec{R}_i}\right) \left(h^{Q}_{z}/h^{Q}\right)^2 F(\beta h^{Q}),$$
$$q^{Q}_{\perp} = \int \Pi_{\mu} dh^{Q}_{z}(\vec{R}_i) \mathcal{P}\left(h^{Q}_{\vec{R}_i}\right) \left\{\left(h^{Q}_{x}\right)^2 + \left(h^{Q}_{y}\right)^2\right\} / (h^{Q})^2 F(\beta h^{Q}). \tag{7}$$

The order parameters averaged over the random distribution of the Weiss fields lead to three different phases: random antiferromagnet with $m^{Q} \neq 0, q^{Q}_{\parallel} \neq 0, q^{Q}_{\perp} = 0$, the spin-glass with $m^{Q} = 0, q^{Q}_{\parallel} = 2q^{Q}_{\perp} \neq 0$, and the mixed antiferromagnetic/spin-glass phase $m^{Q} \neq 0, q^{Q}_{\parallel} \neq 0, q^{Q}_{\perp} \neq 0$. The phase diagram is now given by Eqs. (6) and (7). Mookerjee and Roy[27] have studied the $T = 0$ phases and have shown that there exists a critical concentration x_C which separates the spin-glass from the ordered phases.

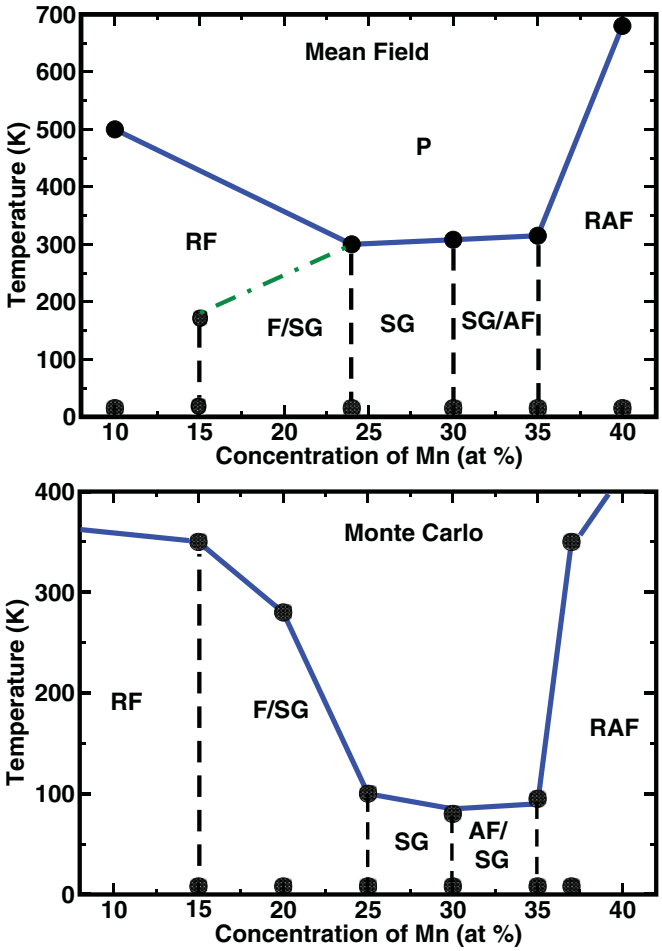

FIG. 16. (Color online) Top: Phase diagram based on a mean-field calculation. Critical temperatures are overestimated. Bottom: The same based on a Monte Carlo estimate. Now critical temperatures and compositions are nearer to experiment.

We have obtained a mean-field calculation of the critical temperatures and obtained the magnetic phase diagram in Fig. 16. If we compare this phase diagram with Fig. 6 we see that our mean-field-based calculation can qualitatively yield phase boundary as a function of Mn concentration with a ferromagnetic phase for $x < 15$, an antiferromagnetic phase for $x > 37$, with glassy phases in between. Of course, it grossly overestimates critical temperatures, which is not surprising for a simple mean-field calculation and the shape of the paramagnetic-spin-glass boundary is rather crudely reproduced.

We followed up the mean-field analysis with a Monte Carlo simulation using the $J^{QQ'}_{ij}$ calculated by us earlier. We note two points: First, the Monte Carlo had to be carried out in a chemically disordered alloy. This is because in the temperature range the magnetic transition takes place, the alloy remains chemically disordered. To obtain a disordered

unit cell, we first calculated the chemical exchange integrals based on a philosophy identical to the magnetic case: starting from a disordered background and embedding an AA, AB, or BB pair configuration before calculating the total energy differences. Having obtained these, we ran a Monte Carlo routine to obtain the disordered background. Finally,we turned on a Monte Carlo analysis of magnetic moments against the random atomic background. The largest simulation cell was $20 \times 20 \times 20$. We ran 10^6 Monte Carlo steps discarding the initial 2×10^5 steps before starting measurement. The critical temperature T_C was calculated from the fourth moment of the averaged magnetization.

Second, Monte Carlo can give us information only across a para-ferro transition. The compositions were so chosen as to be in the region where we have a para to ferromagnetic transition: at compositions with $x = 15,25,30,35$, and 37 at.%. Comparison between Figs. 13 and 16 shows that the Monte Carlo transition temperatures are now quite near the experimental values.

D. Magnetic relaxation

The spin-glass state has a very complex phase space and a lack of ergodicity.[31] This leads to interesting dynamical behavior where relaxation of magnetization is characterized by a wide spectrum of relaxation times.[32] Skubic *et al.*[33] have suggested that magnetic relaxation is an elegant way of exhibiting the multiscale nature of dynamics in a spin glass. The alloy is quenched from a high temperature in zero field, down to temperatures below the critical temperature (T_C or T_g). Relaxation now proceeds during which a small external field h is applied and the subsequent relaxation of magnetization $m(t)$ is measured. After quenching the magnetization first relaxes toward a local equilibrium state. Subsequently, if there is a glassy state present the magnetization proceeds with anomalously slow dynamics. In the absence of a glassy state, the system relaxes toward the global equilibrium state rather fast exponentially. In glassy states this last relaxation is not achievable as the time scale required is greater than the ergodic time $\tau_{\rm erg} \sim \exp N$.

The magnetic pair energies $\mathrm{J}^{QQ'}(R)$ are used to calculate the time-dependent magnetic moment via a Landau-Lifshitz-Gilbert (LLG) equation of motion. This is an important tool to study the existence of the spin-glass phase. We have used an atomistic approach as proposed by Skubic *et al.*[33] Skubic's approach, based on density functional theory, starts with the LLG equation. It allows us to carry out finite-temperature calculations by including a stochastic magnetic field $[\vec{b}_{\vec{R}}(t)]$:

$$\frac{d\vec{m}^{Q}_{\vec{R}}}{dt} = -\gamma \vec{m}^{Q}_{\vec{R}} \times \left(\vec{B}^{Q}_{\vec{R}} + \vec{b}_{\vec{R}}(t)\right) \ldots - \frac{\gamma\alpha}{m}\left[\vec{m}^{Q}_{\vec{R}} \times \left\{\vec{m}^{Q}_{\vec{R}} \times \left(\vec{B}^{Q}_{\vec{R}} + \vec{b}_{\vec{R}}(t)\right)\right\}\right], \quad (8)$$

where the Weiss field

$$\vec{B}^{Q}_{\vec{R}} = -\frac{\partial H}{\partial \vec{m}^{Q}_{\vec{R}}} = -\sum_{Q'} \sum_{\vec{R}' \in Q'} J^{QQ'}_{\vec{R}\vec{R}'}\, \vec{m}^{Q'}_{\vec{R}'} \quad (9)$$

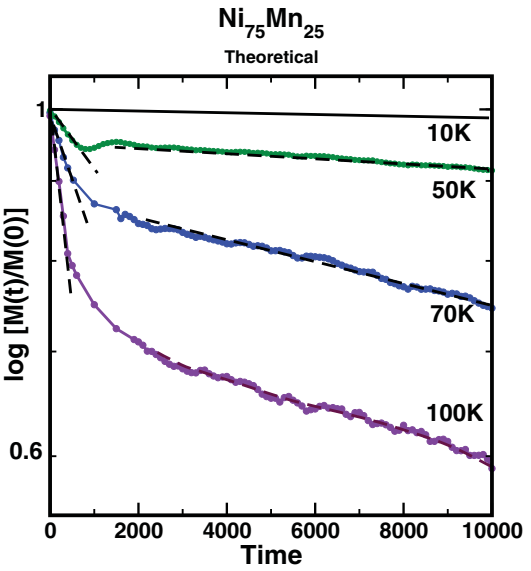

FIG. 17. (Color online) LLG results for the time decay of magnetization for the $Ni_{75}Mn_{25}$ alloy at different temperatures. Here too the alloy magnetization shows anomalously slow relaxation as we approach and cross the glass-transition temperature below 100 K. This is to be compared with Fig. 12.

and the stochastic Gaussian white-noise field describing temperature fluctuations of the Weiss field is

$$\left\langle b^{\mu}_{\vec{R}}(t)\right\rangle = 0, \quad \left\langle b^{\mu}_{\vec{R}}(t) b^{\nu}_{\vec{R}'}(t')\right\rangle = 2D\delta_{\mu\nu}\delta_{\vec{R}\vec{R}'}\delta(t'-t),$$
$$D = \frac{\alpha}{1+\alpha}\frac{k_B T}{\gamma m},$$

where α is the damping parameter associated with D and temperature and m is the magnitude of the magnetic moment. These alloys often exhibit macroscopic magnetic anisotropy in experiments.[34,35] We shall, for the time being, ignore such anisotropy effects, and shall assume that some mechanism exists to provide magnetic damping. This will be parametrized by α. For the present we shall not attempt to obtain this parameter until we have identified the mechanism for damping. We shall set $\alpha = 0.1$. Figure 17 shows the behavior of $\log[M(t)/M(0)]$ vs t at the composition $Ni_{75}Mn_{25}$ at the MCP. The linear fits at small and asymptotic times indicated days at

TABLE II. Experimental and theoretical study of decay of magnetization with time. The decay rates for the initial fast decay and the subsequent decay to a global minimum $[m(t)/m(0) = \exp(-t/\tau)]$ are shown for both the experimental data and LLG simulation results. The alloy shows freezing behavior at low temperatures. The asterisk (*) indicates the fit is a line which is almost horizontal.

	Experimental		LLG	
Temperature (K)	τ_1^{-1}	τ_2^{-1}	τ_1^{-1}	τ_2^{-1}
100	820	93	813	140
70	482	76	449	120
50	245	45	200	41
30	21	10		
10	*	*	*	*

two time scales: a fast decay initially, indicating a decay to a local minimum in the energy landscape. At long times the system slowly relaxes toward the global minimum. Table II shows these decay rates associated with the two relaxation processes just described. This has been done for both the experimental data and the LLG results. We note that across the temperature range they agree rather well, with exponential relaxations at high temperatures to an almost logarithmic relaxation at 10 K. This is a definite signature of the spin-glass phase.

V. CONCLUSIONS

We conclude from a detailed experimental magnetic study of several disordered $Ni_{1-x}Mn_x$ alloys that the spin-glass-like state in these alloys below T_{fg} has a spontaneous (FM) moment. This moment decreases slowly with rising temperature and merges smoothly with the spontaneous moment of the FM state at the multicritical point (MCP) around 25 at.% Mn. The existence of the reentrant SG phase, a canonical SG phase, and the onset of an antiferromagnetic phase around 37 at.% Mn is also confirmed. In brief, we found ferromagnetic LRO with reentrant spin-glass (RSG)/ferro-spin-glass (FSG) phase for $x \leqslant 25$, an antiferromagnetic LRO around $x \sim 37$, and a gradual change from a canonical spin-glass state (which is nothing but a short-range antiferromagnet) to a long-range AF phase in the intermediate composition region.

A first-principles density functional based theory predicts magnetization, as a function of composition, in good agreement with experiment. Since we believe that the spin-glass transition is a dynamic freezing of spin degrees of freedom, we studied magnetization relaxation using a LLG formalism. We showed that in the composition range where experiment observes spin-glassy behavior, we also see anomalously slow relaxation of magnetization.

ACKNOWLEDGMENTS

This work was done under the HYDRA collaboration between our research groups. R.B. thanks Uppsala University for hospitality during the time this work was done. G.C.K. thanks the ICTP for NH-56 Network Program and S. N. Bose Centre for hospitality. P.P. and A.K.M. gratefully acknowledge financial assistance from project No. SR/S2/CMP-18/204 of the Department of Science and Technology, Government of India.

*Present address: Christopher Road H. S. School for Girls, 35 Christopher Road, Kolkata 700014, India.
†S. N. Bose National Centre for Basic Sciences, Kolkata, India.

[1] R. Hahn and E. Kneller, Z. Metallkd. **49**, 426 (1958).
[2] J. S. Kouvel and C. D. Graham, J. Phys. Chem. Solids **11**, 220 (1959).
[3] W. Abdul-Razzaq and J. S. Kouvel, Phys. Rev. B **35**, 1764 (1987).
[4] R. G. Aitken, T. D. Cheung, J. S. Kouvel, and H. Hurdequint, J. Magn. Magn. Mater. **30**, L1 (1982).
[5] J. J. Hauser and J. E. Bernardini, Phys. Rev. B **30**, 3803 (1984).
[6] A. Mookerjee, Pramana **14**, 11 (1980).
[7] M. Gabay and G. Toulouse, Phys. Rev. Lett. **47**, 201 (1981).
[8] W. J. Carr Jr., Phys. Rev. **85**, 590 (1952).
[9] F. Bolzoni and R. Cabassi, Physica B **346-347**, 524 (2004).
[10] J. M. Cowley, Phys. Rev. **77**, 669 (1950).
[11] B. R. Coles, B. V. Sarkissian, and R. H. Taylor, Philos. Mag. B **37**, 489 (1978).
[12] B. H. Verbeek and J. A. Mydosh, J. Phys. F **8**, L109 (1978).
[13] A. K. Majumdar and P. v. Blanckenhagen, Phys. Rev. B **29**, 4079 (1984).
[14] J. A. Mydosh, *Spin Glasses: An Experimental Introduction* (Taylor & Francis, London, 1993).
[15] D. Chowdhury and A. Mookerjee, J. Phys.: Condens. Matter **17**, 5049 (1984)
[16] O. Moze, T. J. Hicks, and P. von Blanckenhagen, J. Magn. Magn. Mater. **42**, 103 (1984).
[17] O. K. Andersen and O. Jepsen, Phys. Rev. Lett. **53**, 2571 (1984).
[18] A. Mookerjee, J. Phys. C **6**, L205 (1973).
[19] A. Mookerjee, in *Electronic Structure of Alloys, Surfaces, and Clusters*, edited by D. D. Sarma and A. Mookerjee (Taylor & Francis, London, 2003).
[20] R. Mills and P. Ratanavararaksa, Phys. Rev. B **18**, 5291 (1978).
[21] S. Ghosh, P. L. Leath, and M. H. Cohen, Phys. Rev. B **66**, 214206 (2002).
[22] Moshiour Rahaman and A. Mookerjee, Phys. Rev. B **79**, 054201 (2009).
[23] N. Beer and D. G. Pettifor, in *Electronic Structure of Complex Systems*, edited by P. Phariseau and W. M. Tammerman (Plenum, New York, 1984), p. 769.
[24] F. Ducastelle and F. Gautier, J. Phys. F **6**, 2039 (1976).
[25] A. I. Lichtenstein, M. I. Katsnelson, V. P. Antropov, and V. A. Gubanov, J. Magn. Magn. Mater. **200**, 148 (1987).
[26] A. I. Liechtenstein, M. I. Katsnelson, and V. A. Gubanov, J. Phys. F: Met. Phys. **14**, L125 (1984).
[27] A. Mookerjee and S. B. Roy, Pramana **24**, 563 (1983).
[28] T. Kaneyoshi, J. Phys. C **9**, L289 (1976).
[29] T. Plefka, J. Phys. F **6**, L327 (1976).
[30] D. J. Thouless, P. W. Anderson, and Palmer, Philos. Mag. **35**, 593 (1977).
[31] R. G. Palmer, Adv. Phys. **31**, 669 (1982).
[32] D. Chowdhury and A. Mookerjee, Phys. Lett. A **99**, 111 (1983); J. Phys. F **14**, 245 (1984).
[33] B. Skubic, J. Hellsvik, L. Nordström, and O. Eriksson, J. Phys.: Condens. Matter **20**, 315203 (2008).
[34] P. Monod and Y. Berthier, J. Magn. Magn. Mater. **15–18**, 149 (1980).
[35] S. Ganguly, M. Costa, A. B. Klautau, A. Bergman, B. Sanyal, A. Mookerjee, and Olle Eriksson, Phys. Rev. B **83**, 094407 (2011).